The orbital kinematics of η Carinae over three periastra with a possible detection of the elusive secondary's motion

Emily Strawn[1], Noel D. Richardson[1],[*] Anthony F. J. Moffat[2], Nour Ibrahim[1,3],
Alexis Lane[1], Connor Pickett[1], André-Nicolas Chené[4], Michael F. Corcoran[5,6],
Augusto Damineli[7], Theodore R. Gull[8,9], D. John Hillier[10], Patrick Morris[11],
Herbert Pablo[12], Joshua D. Thomas[13] Ian R. Stevens[14], Mairan Teodoro[9], Gerd Weigelt[15]

[1] *Embry Riddle Aeronautical University, Department of Physics and Astronomy, 3700 Willow Creek Road, Prescott, AZ 86301, United States*
[2] *Département de physique, Université de Montréal, Complexe des Sciences, 1375 Avenue Thérèse-Lavoie-Roux, Montréal (Qc), H2V 0B3, Canada*
[3] *Department of Astronomy, University of Michigan, 1085 S. University, Ann Arbor, MI 48109, USA*
[4] *NSF's NOIRLab, 670 N. A'ohoku Place, Hilo, Hawai'i, 96720, USA*
[5] *CRESST & X-ray Astrophysics Laboratory, NASA/Goddard Space Flight Center, Greenbelt, MD 20771, USA*
[6] *The Catholic University of America, 620 Michigan Ave., N.E. Washington, DC 20064, USA*
[7] *Universidade de São Paulo, Instituto de Astronomia, Geofísica e Ciências Atmosféricas, Rua do Matão 1226, Cidade Universitária, São Paulo, Brasil*
[8] *Exoplanets & Stellar Astrophysics Laboratory, NASA/Goddard Space Flight Center, Greenbelt, MD 20771, USA*
[9] *Space Telescope Science Institute, 3700 San Martin Drive. Baltimore, MD 21218, USA*
[10] *Department of Physics & Astronomy & Pittsburgh Particle Physics, Astrophysics, & Cosmology Center (PITT PACC),*
University of Pittsburgh, 3941 O'Hara Street, Pittsburgh, PA 15260, USA
[11] *California Institute of Technology, IPAC, M/C 100-22, Pasadena, CA 91125, USA*
[12] *American Association of Variable Star Observers, 49 Bay State Road, Cambridge, MA 02138, USA*
[13] *Department of Physics, Clarkson University, 8 Clarkson Ave, Potsdam, NY 13699, USA*
[14] *School of Physics and Astronomy, University of Birmingham, Birmingham B15 2TT, UK*
[15] *Max Planck Institute for Radio Astronomy, Auf dem Hügel 69, 53121 Bonn, Germany*

ABSTRACT
The binary η Carinae is the closest example of a very massive star, which may have formed through a merger during its Great Eruption in the mid-nineteenth century. We aimed to confirm and improve the kinematics using a spectroscopic data set taken with the CTIO 1.5 m telescope over the time period of 2008–2020, covering three periastron passages of the highly eccentric orbit. We measure line variability of Hα and Hβ, where the radial velocity and orbital kinematics of the primary star were measured from the Hβ emission line using a bisector method. At phases away from periastron, we observed the He II 4686 emission moving opposite the primary star, consistent with a possible Wolf-Rayet companion, although with a seemingly narrow emission line. This could represent the first detection of emission from the companion.

Key words: techniques: spectroscopic — stars: massive — stars: variables: S Doradus — stars: winds, outflows — binaries: spectroscopic — stars: individual: η Carinae

1 INTRODUCTION

The binary star system η Carinae is known for being one of the most massive and luminous binaries in our local galaxy (Davidson & Humphreys 2012). The two stars are locked in a highly eccentric orbit (Damineli 1996a; Damineli et al. 1997). Enveloping these stars is the Homunculus nebula which was formed by a large eruption in the mid-nineteenth century (e.g., Currie et al. 1996). The Great Eruption that formed the Homunculus nebula was recently modeled to be the product of a binary merger in a triple system leading to the current orbit (Portegies Zwart & van den Heuvel 2016; Hirai et al. 2021), supported by light echo observations (e.g., Smith et al. 2018) and an extended central high-mass torus-like struc-

ture surrounding the central binary (Morris et al. 2017). In this scenario, the luminous blue variable primary star is currently orbited by a secondary star that is a classical Wolf-Rayet star, as discussed by Smith et al. (2018). The system began as a hierarchical triple, and mass transfer led to the initial primary becoming a hydrogen-deficient Wolf-Rayet star. Mass transfer causes the orbits to become unstable, which leads to the merger and leaves behind the highly eccentric binary system we see today. An alternate model for the eruption relies on the fact that η Car is a binary in a highly eccentric orbit, and proposes that the periastron events triggered large mass transfer events that caused the eruptions (Kashi & Soker 2010). A similar model was used to explain the much less massive eruption that was seen from the SMC system HD 5980 during its LBV-like outburst (e.g., Koenigsberger et al. 2021).

While the binary nature of the system was inferred by Damineli

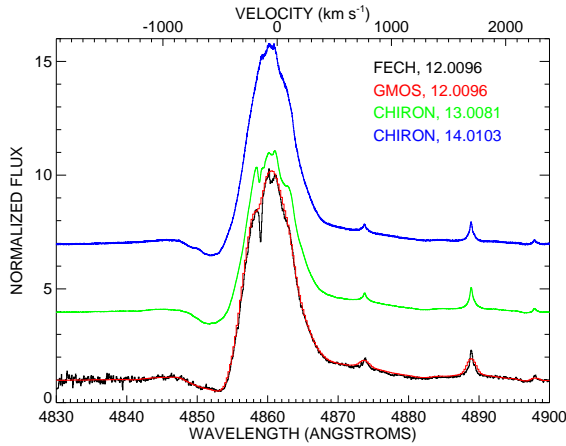[*] E-mail: noel.richardson@erau.edu

Figure 1. A comparison of an example Gemini-GMOS spectrum used by Grant et al. (2020) with the CTIO data from the fiber echelle (FECH) in 2009 and with more recent CHIRON data at the same phase (phases given in the legend). Note that the pixel sizes are indicated for the spectra, which is most obvious for the GMOS spectrum. The spectra are offset by orbital cycle, which highlights the complexities in the echelle spectra compared to the GMOS data.

(1996b) and Damineli et al. (1997), the orbit of the system has mostly eluded observers since the discovery of the spectroscopic events by Damineli (1996a). Davidson (1997) criticized the first orbit published by Damineli et al. (1997) and published a higher eccentricity model using the same data as Damineli et al. (1997). Since these first attempts to derive the orbital motion of the system, very few observationally derived models have appeared in the literature, with most references to the orbit being inferred for modeling purposes. Recently, Grant et al. (2020) used archival moderate-resolution Gemini/GMOS spectra from 2009 to fit the hydrogen lines using multiple, weighted Gaussians to measure radial velocities corrected to account for motion from strong stellar winds. They derived a single-lined spectroscopic orbit based on the upper Balmer lines to be $T_0 = 2454848$ (HJD), $e = 0.91$, $K_1 = 69$ km s^{-1}, and $\omega_{\rm pri} = 241°$ with the period of 2022.7 d that has been widely adopted based on multi-wavelength observations (e.g., Teodoro et al. 2016). These are broadly consistent with the smoothed-particle hydrodynamical (SPH) models used to describe variability across the electromagnetic spectrum (e.g., Madura et al. 2013) including the X-ray light curves (e.g., Okazaki et al. 2008), optical He I absorption variability (Richardson et al. 2016), and the near-UV emission observed with the *Hubble Space Telescope* (Madura & Groh 2012).

While the results of Grant et al. (2020) establish the orbital parameters with greater precision to date, there are potential issues with the determination of orbital elements from hydrogen lines in η Car's spectrum, as the strong wind of the primary causes the effective photospheric radius to be further out from the central star for lower energy transitions. Indeed, Grant et al. (2020) found better results with higher-order Balmer lines than with the optically thick Hα or Hβ. This is a known effect for evolved Wolf-Rayet stars, where the observed semi-amplitude can change with the ionization potential of the line measured because lower-energy emission lines tend to form further out in the wind, where they are more likely to be perturbed by the companion star as seen in γ^2 Vel (Richardson et al. 2017). This effect causes differences from the true orbital motion for lower energy transitions, making it difficult to determine accurate orbits (Grant et al. 2020). Grant & Blundell (2022) confirmed

that their methods used for emission-line stars worked for the WR binaries WR 133 and WR 140 that have combined spectroscopic and interferometric orbits (Richardson et al. 2021; Thomas et al. 2021).

The primary star in the η Car system is a luminous blue variable star, with the largest measured value for a mass-loss rate for a massive star with $\dot{M} = 8.5 \times 10^{-4} M_\odot \rm yr^{-1}$ and a terminal wind speed of $v_\infty = 420$ km s^{-1} (Davidson & Humphreys 1997; Groh et al. 2012). Prior to the recent kinematic studies of Grant et al. (2020) and Grant & Blundell (2022), the best constraints on the companion star parameters, while indirect, came from the X-ray variability analyses from *RXTE*, *Swift*, and *NICER* observations of the system (Corcoran et al. 2001, 2017; Espinoza-Galeas et al. 2022). These analyses point to a secondary star with a mass-loss rate on the order of $\dot{M} \sim 10^{-5} M_\odot \rm yr^{-1}$ and a terminal velocity of $v_\infty \sim 3000$ km s^{-1} (Pittard & Corcoran 2002). These values are broadly in agreement with the suggestion based on the merger models and mass-loss parameters that the remaining secondary would be a Wolf-Rayet star. Despite recent work with long-baseline near-infrared interferometry by Weigelt et al. (2021), no direct detection of the companion star has been made to date. From the interferometric data, a minimum primary-secondary flux ratio of ~50 was derived in the K-band (Weigelt et al. 2007). Given the extreme luminosity of the LBV primary, this is consistent with any O or WR star in the Galaxy.

The evolution of the secondary star may well have been significantly modified by interactions and mass exchange during formation of the present-day binary, but if the current secondary star is a classical H-free Wolf-Rayet star as suggested by Smith et al. (2018) and Hirai et al. (2021), or a hydrogen-rich WNh star, possibly the best line to detect it in the optical would be the He II λ 4686 line, which is the dominant line in the optical for the nitrogen-rich WR stars, or the hydrogen-rich WNh stars. Most of the observations of He II were made near periastron, where the He II excess can be explained by ionization of He I in the colliding winds in a highly eccentric binary. Teodoro et al. (2016) showed that the variability could be explained with the smoothed-particle hydrodynamics models of Madura et al. (2013). Away from periastron ($0.04 < \phi < 0.96$), the He II line is typically not observed with moderate resolving power and a nominal S/N of ~100.

In this paper, we present our analysis of the spectroscopy collected with the CTIO 1.5 m telescope and the CHIRON spectrograph, as well as the data collected with the previous spectrograph on that telescope with the aim of better constraining the kinematics of the system. These observations are described in Section 2. In Section 3, we review the variability in the two Balmer lines we can easily measure (Hα and Hβ). Section 4 describes our techniques of measuring the radial velocity of the Hβ line, and presents observations of He II away from periastron in the hope of determining the orbit of the companion star. We discuss our findings in Section 6, and conclude this study in Section 7.

2 OBSERVATIONS

We collected high resolution spectra of η Carinae during the periastron passages of 2009, 2014, and 2020. Many additional spectra were taken in the intermediate phases of the binary orbit as well. These were collected from the 1.5m telescope at Cerro Tololo Inter-American Observatory (CTIO 1.5) and both current CHIRON and the former fiber-fed echelle spectrograph (FECH). The data from the 2009 spectroscopic event spanned from 2008 October 16 to 2010 March 28, with approximately one spectrum taken every night between 2008 December 18 to 2009 February 19, which were previ-

ously used by Richardson et al. (2010, 2015) and cover the spectral range ∼ 4700 − −7200Å. These spectra with the fiber echelle[1] were collected in late 2009 and 2010, and often had a signal-to-noise ratio around 80–100 per resolution element with $R \sim 40,000$. In total, we analyzed 406 spectra of the system.

The 2014–2020 data were collected with the new CHIRON spectrograph (Tokovinin et al. 2013), and spanned the time between 2012 March 2 and 2020 March 16, with high-cadence time-series spanning the 2014 and 2020 periastron passages between 2013 December 29 through 2015 April 21 as well as between 2020 January 3 to 2020 March 16 when the telescope shut down for the COVID-19 pandemic. The CHIRON spectra cover the spectral range of ∼4500-8000Å, with some spectral gaps between orders in the red portion of the spectrum. The data covering the 2014 periastron passage were previously used by both Richardson et al. (2016) and Teodoro et al. (2016). These data have a spectral resolution of $R \sim 80,000$ and typically have a signal-to-noise of 150–200 in the continuum and were all reduced with the CHIRON pipeline, which is most recently described by Paredes et al. (2021). In addition to the pipeline reductions, we perform a blaze correction using fits from an A0V star, as done by Richardson et al. (2016), allowing orders to be merged if needed. This process resulted in a flat continuum in regions that were line-free.

These observations were all fiber-fed with the fiber spanning 2.7″ on the sky, meaning that the data include the nebular emission from the Homunculus nebula formed from the eruption of η Car in the mid-nineteenth century, as well as the Weigelt knots (Weigelt & Ebersberger 1986) that are thought to have originated from the second eruption in the 1890s. The CHIRON spectra are normalized through a comparison with a measured blaze function from the star HR 4468 (B9.5V), as was done in the analysis of Richardson et al. (2016). Example spectra are shown in Figure. 1, with a comparison to a spectrum used by Grant et al. (2020) and Grant & Blundell (2022).

3 MEASURED VARIABILITY IN THE BALMER LINES, Hα AND Hβ

Our observations are unique in providing both the spectral resolution and signal-to-noise to measure the line strength (equivalent width) and profile morphology of the emitting gas for the Hα and Hβ lines of η Carinae. Here, we detail the observations of the variability of the hydrogen lines. We estimate errors on equivalent width using the methods of Vollmann & Eversberg (2006). We note that the analysis of Richardson et al. (2015) includes many optical wind lines near the 2009 periastron passage and phases far from periastron. These line profiles all show minimum line strength near periastron as the secondary's high ionizing radiation goes behind the primary star's optically thick wind. We use a phase convention in which the low-ionization state observed by Gaviola (1953) in 1948 is deemed to be cycle 1, so that the low-ionization state starting in Feb. 2020 marks the start of cycle 14. We leave the kinematics analysis of the metal lines for a future analysis in order to confirm the results of Grant et al. (2020) and Grant & Blundell (2022) here, with plans of using higher signal-to-noise spectra in a future analysis.

3.1 Hα

Richardson et al. (2010) examined the variability of the Hα profile of η Carinae across the 2009 periastron passage. They found that the profile's strength decreased during the periastron passage and reached a minimum a few days following the X-ray minimum. They postulated that the changes were caused by the drop in the ionizing flux from the secondary when the companion moved to the far side. In addition, they observed an appearance of a P Cygni absorption profile and an absorption component at −145 km s^{-1}, that also appeared as the secondary's ionizing radiation was blocked by the primary star's optically thick wind. Richardson et al. (2015) expanded upon this model to describe the variations of the optical He I profiles while documenting the variability of the optical wind lines across the 2009 periastron passage.

We measured the equivalent width of Hα for all of our spectra in the range 6500 – 6650Å. These results are shown in Fig. 2, where we show the measurements both compared to time and to binary phase, assuming a period of 2022.7 d, and the epoch point given by Teodoro et al. (2016), which represents the time of the periastron passage based on a comparison of the He II observations (Teodoro et al. 2016) to SPH models of the colliding winds. Broadly speaking, the strength of the line relative to the locally normalized continuum shows a fast decrease and recovery near each periastron passage. Richardson et al. (2010) found that the variability is smoother when considering the photometric flux in the determination of the equivalent widths. We did not make this correction in these data, but do see the similarities of the events in the context of the raw equivalent widths.

There is no strong long-term variability in these observations, and the 2014 and 2020 observations were nearly identical in their variations. Recently, Damineli et al. (2019, 2021) found that there are long-term brightness and spectral changes of the system that has been ongoing for decades and accelerated since the mid-1990s, but now seems to be stabilizing. The shape of the Hα variability has remained similar over these three well-observed periastron passages, and the line strength has stabilized across the past two cycles, which could indicate that the system is mostly stable aside from the binary-induced variability.

Richardson et al. (2010) also documented the timing of the appearance of the P Cygni absorption component for Hα. In the 2009 observations we see the absorption occurring at approximately HJD 2454840.7 ($\phi \approx 12.00$) and still persisting through the last observation, 2454881.7 ($\phi \approx 12.02$). In 2014 a P Cygni absorption occurs at 2456874.5 ($\phi \approx 13.00$) persisting until the object was not observable at HJD 2456887.5 ($\phi \approx 13.01$). In 2020, the absorption is seen at 2458886.8 ($\phi \approx 14.01$) and still detected through the last observation on HJD 2458925.0 ($\phi \approx 14.02$).

A narrow absorption component was observed near −145 km s^{-1} in the 2009 observations (Richardson et al. 2010) from 2454836.7 ($\phi \approx 12.00$) through the last day of observation, 2454881.7 ($\phi \approx 12.02$). In 2014 an absorption in the same location is observed from 2456863.5 ($\phi \approx 13.00$) – 2456977.8 ($\phi \approx 13.06$). There is no absorption at this location strong enough to make a definitive detection in 2020. Pickett et al. (2022) documented the changes in absorption behavior for the Na D complex at these velocities, showing that the absorption from these components associated with the Little Homunculus, formed during the second eruption in the 1890s, are weakening with time and moving to bluer velocities.
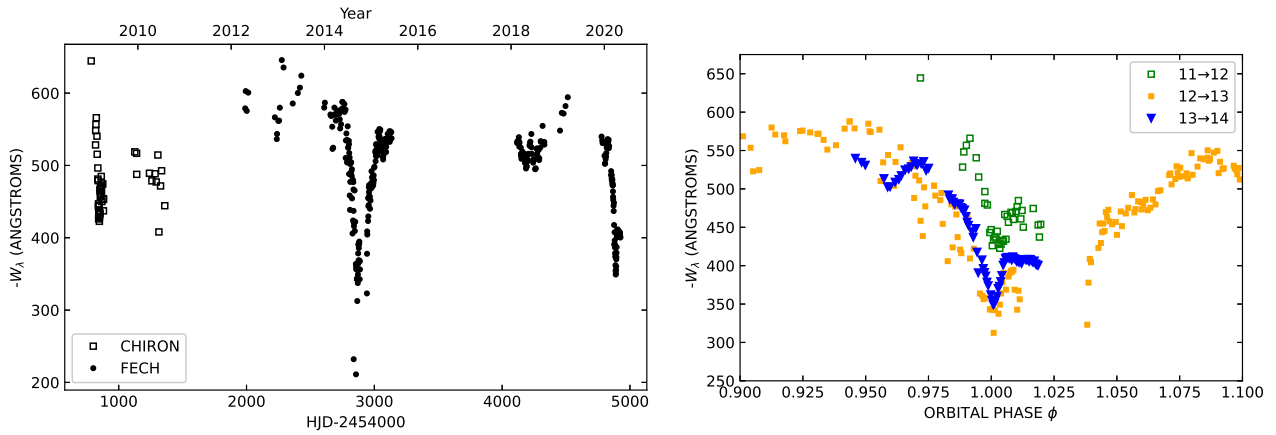
Figure 2. Variation in Hα emission line with respect to time (left) and phase (right); with the data taken between October 2008 and March 2020. Data taken from the previous echelle spectrograph is indicated by open squares and data from the new CHIRON spectrograph is indicated by solid dots. In the phase plot, we show the different cycles in different colors to clarify the timing of each data set. Furthermore, the errors are typically the size of the points or smaller. The phase convention shown in the right panel references the low-ionization spectrum near periastron first observed by Gaviola (1953).
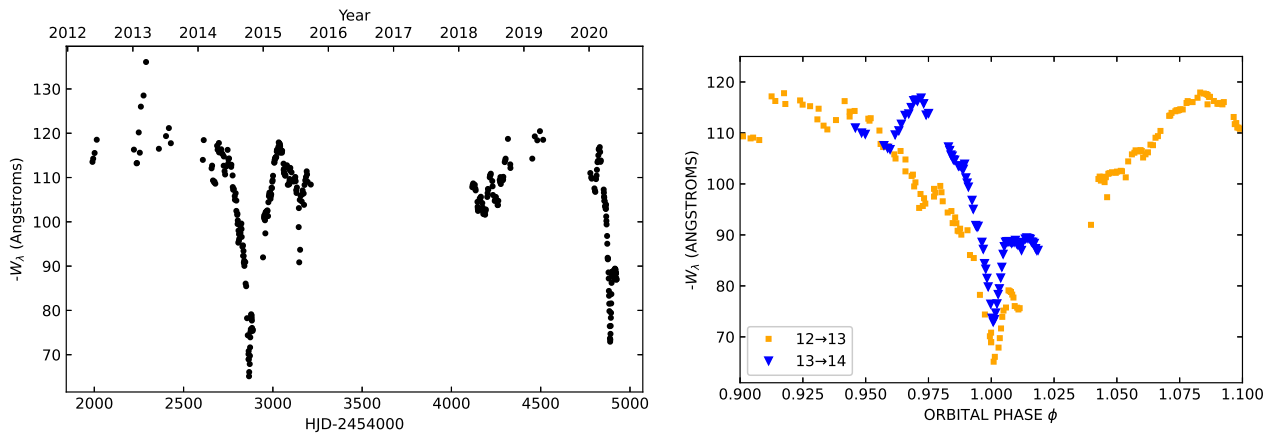
Figure 3. Variation in Hβ emission line with respect to time (left) and phase (right); with the data taken with CHIRON spectrograph as the FECH data were too noisy to determine equivalent widths. In the phase plot, we show the two recent cycles in different colors to clarify the timing of each data set. Furthermore, the errors are typically the size of the points or smaller. The phase convention shown in the right panel references the low-ionization spectrum near periastron first observed by Gaviola (1953).

3.2 Hβ

While some of the Hβ variability was documented for the 2009 periastron passage of η Car by Richardson et al. (2015), the full variability and timing of the changes is still not well documented in the literature. The lack of a more quantitative assessment of the variability is in part due to the lower signal-to-noise in the Hβ data from the 2009 event. Similar to the Hα profile, Hβ experiences a P Cygni type absorption near −500 km s^{-1} near periastron. We note the absorption appears in 2009 at approximately HJD 2454837.7 ($\phi \approx$ 12.00) and persist through the last observation taken on 2454879.7 ($\phi \approx$ 12.01). In 2014, it appears at approximately 2456863.6 ($\phi \approx$ 13.00) and ends during a seasonal gap in observations beginning at 2456887.5 ($\phi \approx$ 13.01). In 2020, the P Cygni absorption is observed between 2458886.8 ($\phi \approx$ 14.00) and continues through the last day of observations on 2458925.0 ($\phi \approx$ 14.02). This transient absorption was determined to be originating from the downstream bowshock by Gull et al. (2022).

A narrow absorption component, previously observed by Richardson et al. (2015), is detected near −145 km s^{-1} in the 2009

observations from 2454837.7 ($\phi \approx$ 12.00) and proceeds through the end of observations on 2452879.7 ($\phi \approx$ 12.01). In 2014, this absorption is observed between 2456864.5 ($\phi \approx$ 13.00) and also persists through the last day of observations 2456887.5 ($\phi \approx$ 13.01). As with Hα, there is no discernible absorption at −145 km s^{-1} in 2020 observations.

Figure 3 shows the time series variation in the Hβ equivalent width over the last two periastron cycles. We note that the 2009 observations are not included as they are recorded with the former echelle spectrograph and have lower signal-to-noise, though the appearance of the P Cygni absorption remains reliable. As with the Hα equivalent widths, there is a consistency in the decrease in equivalent width for the time period corresponding to times close to periastron.

4 LINE KINEMATICS

We measured the bisector velocity of Hβ and the centroid position of the He II λ4686 line. Hβ measurements were taken during the 2009, 2014, and 2020 periastron events and the He II 4686 measurements
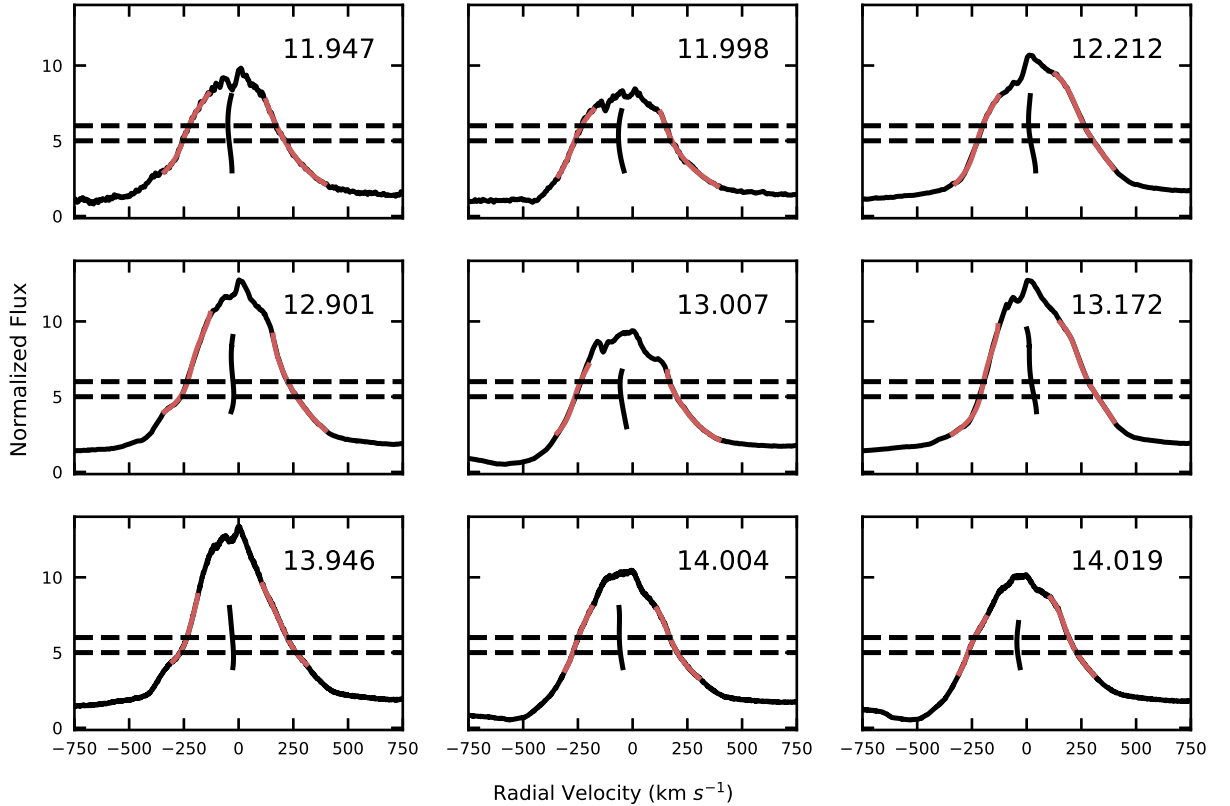
Figure 4. Example polynomial fits to Hβ emission lines from 2009, 2014, and 2020 periastron events. The profiles are shown in black with the portion of the line wings fit with a polynomial shown in red. The bisector velocity is shown as a vertical line corresponding to the normalized flux at the same level as the measurements. Near the edges of these ranges, the bisector often appears to curve due to either profile asymmetries or larger errors in the polynomial fits. The bisector velocities between normalized flux levels of 5 and 6, indicated by the dashed lines, were averaged to obtain a final relative velocity for each day. Further details are given in Section 4.1.

were taken for 2014 and 2018 and do not include time within $\phi = 0.95 - 1.05$ to avoid observations affected by periastron caused by colliding-wind effects which, to first order, behave with a D^{-1} trend for adiabatic and D^{-2} or steeper for radiative conditions, where D is the orbital separation, which is small and quickly changing at periastron. Teodoro et al. (2016) show the behavior of the He II 4686 line near periastron in detail. All measurements are tabulated in online supplementary data.

4.1 Bisector velocities of Hβ

The process used to find the bisector velocity of Hβ is demonstrated in Fig. 4. Grant et al. (2020) and Grant & Blundell (2022) used a method of Gaussian decomposition using many components to moderate-resolution spectroscopy taken with Gemini-South and GMOS. Their GMOS spectra of η Car are limited in that the highest resolving power available is ~ 4400, whereas our spectroscopy has a resolving power of 40,000 from the fiber echelle, and 80,000 for the CHIRON data. The profiles become more complex at higher spectral resolution, making this multiple-Gaussian method more difficult to

implement, likely requiring more than twice as many components compared to the work of Grant et al. (2020).

In order to create a simpler measurement that has reproducible results for any spectroscopic data set, we implemented a bisector technique. We began by fitting two fourth degree polynomials, one to the red side and another on the blue side of the profile in order to smooth over any noise inherent in the data. Through this fit, we were then able to establish the bisecting velocity position at each emission level with higher precision. Example fits are shown in red in Fig. 4. In the regions of heights of 4× the continuum up to 10× the continuum, we calculate the bisecting velocity. This area was chosen based on the relatively vertical nature of the bisector in this region. We then created comparisons of all spectra and found that the bisecting line was nearly always vertical in the region of 5 − 6× the normalized continuum. We therefore used this region, measuring the velocity at every 0.1 increment between these values, and adopting an average measurement as the radial velocity for the spectrum. The choice of a common emission height with which to measure the bisector velocities allows us confidence in the results as it would relate to gas emitting from the same region for all spectra, whether the line is weak or strong in that particular observation. The resulting velocities
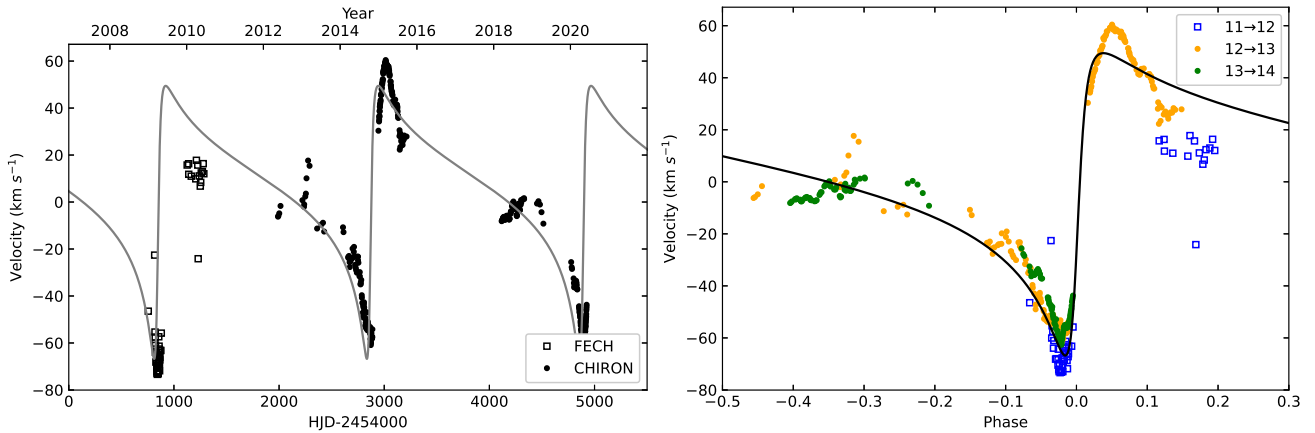
Figure 5. Radial velocities from Hβ bisector measurements compared to time (left) and orbital phase (right). The orbital fit is described in Section 4.3 and typical errors are on the order of the size of the points.
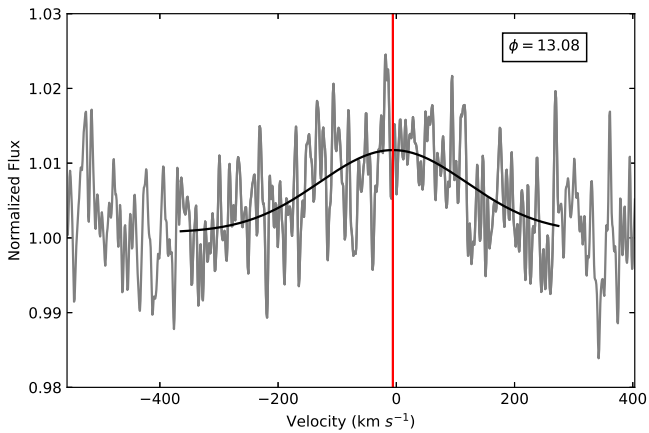

Figure 6. Gaussian fit to an example He ɪɪ emission line with a vertical line plotted at the fitted peak. This particular spectrum had a signal-to-noise ratio of 210 per resolution element.

are shown in Fig. 5. We provide this bisector code via GitHub[2] for future use on comparable datasets.

4.2 He ɪɪ λ4686

The region surrounding, but not blended with, the He ɪɪ λ4686 transition is complicated by several features including narrow emission lines from the Weigelt knots (Weigelt & Ebersberger 1986) along with wind emission from Fe ɪɪ and He ɪ lines (for a figure showing that region of the spectrum, see Teodoro et al. 2016). While these do not directly overlap with the core of the He ɪɪ line, they can complicate this fitting if not properly avoided. The He ɪɪ λ4686 line has usually been observed near periastron passage when the line is dominated by the wind-wind collisions, which has been documented and modeled by Teodoro et al. (2016). The line was discovered by Steiner & Damineli (2004). Since then, multiple studies have attempted to explain the formation of the stronger line observed near periastron ($L_{He \, ii} \sim 300 \, L_\odot$; Martin et al. 2006; Mehner et al. 2011, 2015; Teodoro et al. 2012; Davidson et al. 2015), but the colliding

[2] https://github.com/EmilysCode/Radial-Velocity-from-a-Polynomial-Fit-Bisector.git

wind model best reproduces the emission near periastron. This emission is strongest for times within ±0.05 in phase from periastron, as detailed in the recent analysis of Teodoro et al. (2016).

Outside of the phase intervals near periastron, the He ɪɪ λ4686 line could only be properly observed with high spectral resolution and high signal-to-noise data (Teodoro et al. 2016). Our data taken with CHIRON, after the 2014 periastron passage has the necessary sensitivity to detect this notably weak emission line. We measure the radial velocity of this line outside of $\phi = \pm 0.05$ of periastron, so that it minimizes the effects of the colliding winds that peak at periastron.

As shown in Fig. 6, we fit a Gaussian to the He ɪɪ emission line and use the centroid position to determine the radial velocity. Unfortunately, the continuum placement for the feature is not reliable enough to measure equivalent widths with precision, but the line was nearly constant in equivalent width when considering the errors of these measurements. Before fitting the 2018 observations near apastron, we needed to average up to ten observations to improve the signal-to-noise ratio. The resulting velocities are shown in Fig. 7 with a resulting total of 19 data points. The averaging of the points from the 2018 data resulted in a smaller dispersion of the data than seen in the earlier points.

The He ɪɪ line is normally absent in the spectra of luminous blue variables. The extreme mass-loss rate of η Car does not preclude this emission line originating in the primary star's wind, as there are some combinations of parameters used that can create this weak emission feature in CMFGEN models. These models and parameters are very sensitive and depend on the mass-loss rate and stellar radii used. The He ɪɪ can be formed through strong wind collisions at times close to periastron (e.g., Teodoro et al. 2016). However, this line moves in opposition to the primary star's motion, so we consider this feature as originating from the companion during these phases far from periastron for the remainder of this analysis.

4.3 Orbital Kinematics and Observed Elements

We began our fit of the kinematics of the primary star with the `BinaryStarSolver` software (Milson et al. 2020; Barton & Milson 2020). The resulting orbit is broadly in agreement with the orbit derived with Hβ velocities by Grant et al. (2020), with the orbital elements given in Table 1. Our resulting fits are in agreement with those of Grant et al. (2020) so we did not perform the same correction for the stellar wind effects as in their analysis.

Line	T_0 (HJD-2400000)	e	K (km s^{-1})	ω (degrees)	γ (km s^{-1})	Source
Paγ	48800 ± 33	0.63 ± 0.08	53 ± 6	286 ± 6	-15 ± 3	Damineli et al. (1997)
Paγ, He I 6678	48829 ± 8	0.802 ± 0.033	65.4 ± 3.5	286 ± 8	-12.1 ± 2.7	Davidson (1997)
Paγ, Paδ	50861	0.75	50	275	-12	Damineli et al. (2000)
Hβ	$54854.9^{+4.5}_{-4.1}$	0.82 ± 0.02	$53.0^{+2.1}_{-1.9}$	254 ± 4	-25.5 ± 2.0	Grant et al. (2020)
All Balmer lines	54848.3 ± 0.4	0.91 ± 0.00	69.0 ± 0.9	241 ± 1	. . .	Grant et al. (2020)
Upper Balmer lines	54848.4 ± 0.4	0.89 ± 0.00	69.9 ± 0.8	246 ± 1	. . .	Grant et al. (2020)
Hβ	56912.2 ± 0.3	0.8100 ± 0.0007	58.13 ± 0.08	251.43 ± 0.19	6.34 ± 0.10	This work(BinaryStarSolver)
Hβ	56927.4 ± 0.5	0.8041 ± 0.0008	54.6 ± 0.2	260.6 ± 0.2	4.83 ± 0.09	This work (PHOEBE)
He II	56973.5 ± 0.2	0.937 ± 0.001	129.5 ± 5.0	80.6 (fixed)	63.1 ± 0.4	This work

Table 1. Orbital elements from previous publications and the results from this work. For the orbits of Grant et al. (2020), Grant & Blundell (2022), and our work, the period has been held constant at 2022.7 d, while it was fit in the earlier work of Damineli et al. (1997), Davidson (1997), and Damineli et al. (2000) with periods that agree with 2022.7 d within their errors. Note that our errors from the PHOEBE code may be underestimated, especially for the He II line (see text for details).
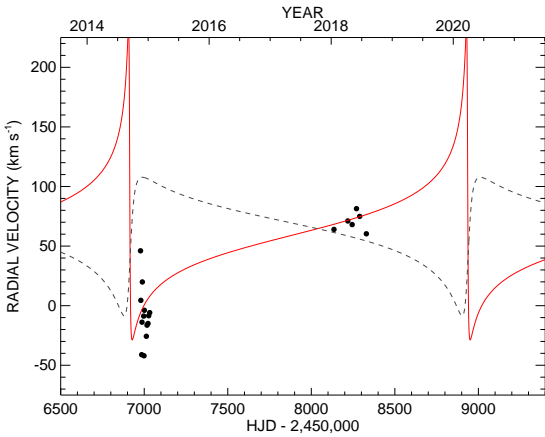

Figure 7. Radial velocity as determined using centroid positions in He II emission at phases away from periastron during 2014–2018 with CHIRON. We overplotted the He II orbit from Table 1, along with the Hβ solution from our work shifted to the same γ-velocity as the He II orbit as a grey dashed line.

In an attempt to fully assess the errors of the parameters, we used the PHOEBE code (PHysics Of Eclipsing BinariEs; Prša & Zwitter 2005; Prša et al. 2016) to verify the orbital elements. The latest version of PHOEBE incorporates the Markov Chain Monte Carlo package emcee (Foreman-Mackey et al. 2013). Unlike traditional orbit fitting routines, PHOEBE fits using the variable of the projected semi-major axis ($a \sin i$) rather than the semi-amplitude K, but these are easily interchangeable using

$$a \sin i = \frac{(1 - e^2)^{1/2}}{2\pi} KP.$$

These orbital elements are also similar to the other published orbital elements measured with Hβ, and the resulting orbit is shown in Fig. 5. The distribution of the errors from the Monte Carlo simulation, shown in Fig. 8, is tightly constrained but shows that various orbital elements have errors that are interdependent with other parameters. While this represents the best solution to the entire data set, we explored how the parameters change if we kept only the densest of the three periastra observed (the 2014 event). Running the PHOEBE code with the MCMC package on just those data resulted in the eccentricity being slightly larger ($e = 0.824$), the time of periastron being later (HJD 2,456,935.31), and the value of $a \sin i$ (hence K_1) being slightly larger at 2620.4 $R_\odot$. These values are outside the

limits given with our MCMC fit of all of the data, so we caution that the errors in Table 1 are likely underestimated. We include the fit parameters in the same style as Fig. 8 in the online Fig. A1.

Once the orbital elements for Hβ were fit, we proceeded to run a simpler model for the He II emission. For this PHOEBE model, we keep ω constant to that representing the primary star from the upper Balmer line results from Grant et al. (2020). However, we do allow the semi-major axis, γ-velocity, e, and time of periastron passage to vary. The resulting orbit is more eccentric than that of the primary star when derived using Hβ (and a bit more eccentric than the Grant et al. (2020) solution) and is shown in Fig. 7. With future observations of the He II line at times away from periastron, a combined double-lined orbit of the system with ω being consistent for the two stars will be possible.

5 DISCUSSION

The optical spectrum of η Car is dominated by emission lines from the wind of the primary and its ejecta. The dominant emission lines are the hydrogen Balmer lines, but there are strong lines from He I and Fe II in the spectrum as well. The He I lines, when considered in non-LTE stellar wind models, are a strong function of the adopted value of the stellar radius. However, if most of the He I emission comes from the colliding wind interaction region, it forces a larger stellar core radius value for the primary star, $\sim 120R_\odot$ in the preferred models (see Hillier et al. 2001, for many further details). The model of Groh et al. (2012) improved previous spherically symmetric models of Hillier et al. (2001) in that the spectrum was modeled with a cavity carved from the wind of the secondary, which was included along with a central occulter or "coronagraph" that extended $\sim 0.033''$ to allow for stronger He I emission, and better agreement for the P Cygni absorption lines. Given the spectral modeling agreement for the spectroscopically similar star HDE 316285 (Hillier et al. 1998), the strong disagreements for the absorption components and He I lines led to an interpretation that the He I lines are formed in the wind-wind collision region of the system (Nielsen et al. 2007). Indeed, the P Cygni absorption component variability of the optical He I lines seems to represent the outflowing shocked gas from the wind-wind collision region (Richardson et al. 2016). These results all indicate that the best lines in the optical for determination of the orbit may indeed be the upper hydrogen Balmer lines, even if they are likely modified by the wind collisions.

All of the measured orbits, including ours, rely on measurements taken when the line profiles are most variable near periastron. This
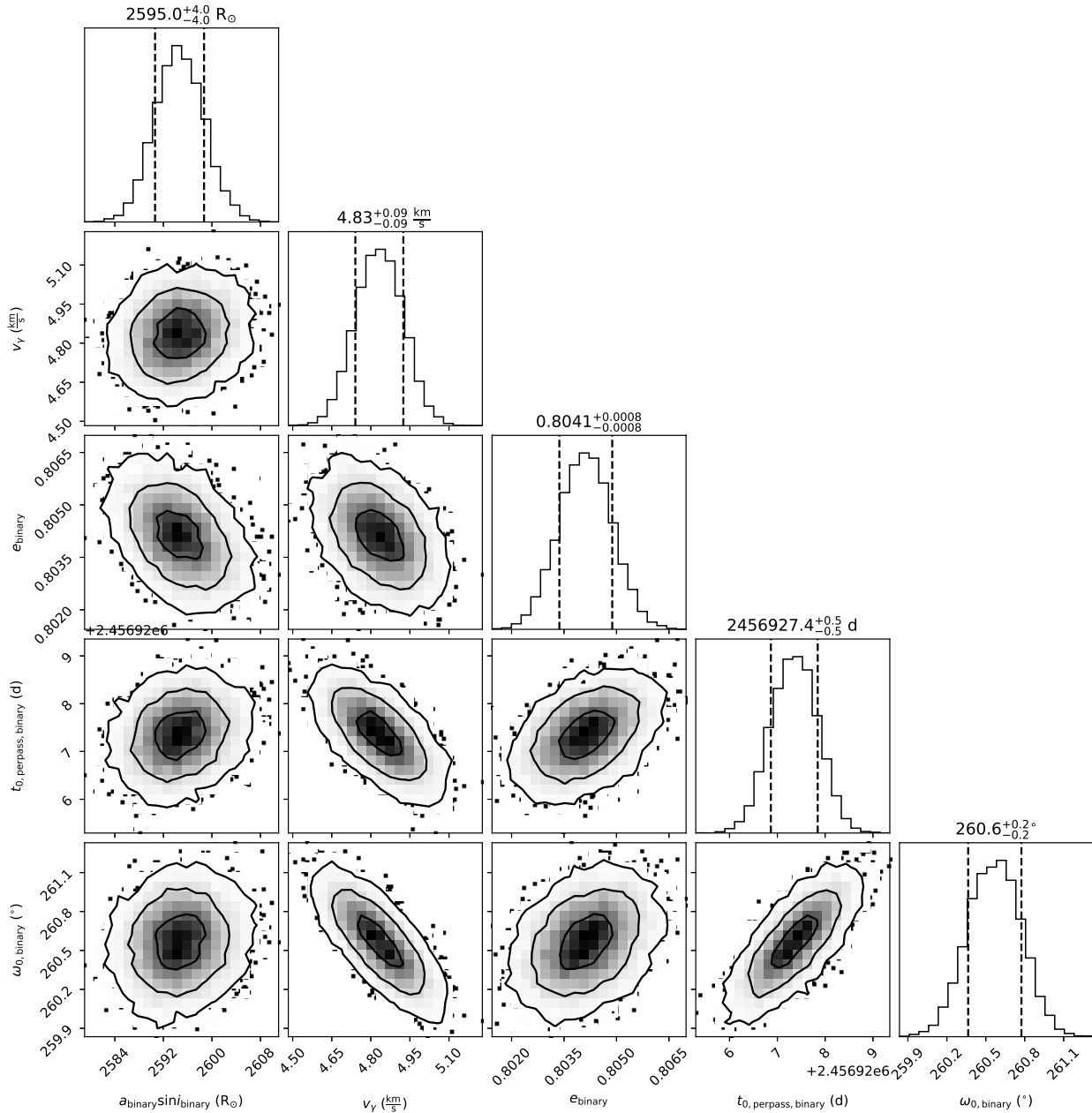
Figure 8. Results of the Markov chain Monte Carlo fit for the Hβ velocities. Note that ω_0 refers to the value of ω for the primary star.

likely causes additional errors in the parameters derived, but we tried to always sample emission from the same line formation region by taking bisector velocities at the same height. Furthermore, our technique produces nearly the same orbital elements as those from Grant et al. (2020) in the case of Hβ. Grant et al. (2020) proceeded to correct the orbital elements by considering the effects of the outflowing wind.

These results all show that the system is a long-period and highly eccentric binary where the primary star is in front of the secondary at periastron, causing the ionization in our line of sight to drop during the "spectroscopic events" due to a wind occultation of the secondary at these times. The results of Grant et al. (2020) show that the higher-order Balmer lines give different results than that of the lower-level lines such as Hα or Hβ, which is expected as the higher

level lines form deeper in the wind (e.g. Hillier et al. 2001). As such, the results of Grant et al. (2020) and Grant & Blundell (2022) should be considered the best for the primary star at the current time. Similar differences in the orbital kinematics is sometimes inferred for Wolf-Rayet stars (e.g., γ^2 Vel; Richardson et al. 2017).

Despite the detection of the He II λ4686 emission at times near apastron by Teodoro et al. (2016), the exact formation channel for this line remains unclear. The emission lines in colliding wind binaries often vary as a function of the orbit due to the colliding wind line excess (e.g., Hill et al. 2000), and the modeling of these variations has been done in the context of the so-called Lührs model (Lührs 1997). Recently, the excess emission was observed to be a strong cooling contributor when X-ray cooling becomes less efficient in the colliding wind binary WR 140 (Pollock et al. 2021). In WR 140, the

Lührs model was used by Fahed et al. (2011) to explain the variations in the C III λ5696 line near periastron.

The Lührs model can explain changes in the radial velocity and the width of the excess emission. As can be seen in Fig. 6, we detect the He II line with our spectra, but the actual characterization of this line will have large errors in line width due to the limited signal-to-noise for the detection in the spectroscopy. We used the models for WR 140 (Fahed et al. 2011) as a starting point, changing stellar and binary parameters as appropriate to the η Carinae system to investigate if the He II velocities in Fig. 7 were from colliding wind excess emission. For the velocity of the outflow, we can see that during the periastron passage of 2014, η Car's outflow reached velocities faster than the primary star's wind speed based on the optical He I lines (Richardson et al. 2016), which are slower than the excess absorption seen to reach nearly 2000 km s^{-1} in the meta-stable He I λ10830 line (Groh et al. 2010). With these velocities, we expect to see the observed amplitude of the excess increase between the times of 2015 and 2018 like we see in Fig. 7, but with amplitudes of at least 1000 km s^{-1}, much greater than the ∼ 100 km s^{-1} observed.

Therefore, the analysis of the He II λ4686 emission line at times away from periastron from the CHIRON spectra is an important observation towards understanding the nature of the companion. We note that the data indicate a narrower emission line profile then expected from the parameters inferred for the secondary. However, the primary star dominates the spectrum, and the motion of this peak opposite the primary indicate that the He II excess could be from the secondary's wind. In particular, the Lührs models of the kinematics of the He II line seem to exclude the possibility that the line is formed in the colliding winds at times away from periastron.

The models of Smith et al. (2018) suggest that the companion should be a classical Wolf-Rayet star. The classical hydrogen-free Wolf-Rayet stars can be split into the WN and WC subtypes. The WN stars show strong He and N lines, with the He II λ4686 typically being the strongest optical line, whereas the WC subtype exhibits strong He, C, and O lines with the C IV λλ5802,5812 doublet often being the strongest optical line. There is also the rare WO subtype, which is similar to the WC subtype but shows more dominant O lines. The WO stars were recently shown to have higher carbon and lower helium content than the WC stars, likely representing the final stages of the WR evolution (Tramper et al. 2015; Aadland et al. 2022). Given the generalized characteristics of WR stars, a WN star would seem the most likely companion star if the He II λ4686 line is from the companion at times further from periastron.

For contrast, the Carina nebula is also the home to several hydrogen-rich Wolf-Rayet stars: WR 22, WR 24, and WR 25 (Rosslowe & Crowther 2015)[3]. This type of WR star tends to be considered the higher mass and luminosity extension of the main sequence. As such, these stars have masses in excess of ∼ 60$M_\odot$, with the R145 system in the LMC having masses of the two WNh stars being 105 and 95 $M_\odot$ (Shenar et al. 2017). Like the classical WN stars, these stars have similar nitrogen and helium spectra, along with stronger emission blended on the Balmer lines which overlap with Pickering He II lines. The region surrounding the He II λ5411 line in our η Carinae spectra does not exhibit emission lines at the same epochs as our observations of He II 4686, making it difficult to quantify the companion's properties without the higher order He II lines which would also be notably weaker than He II λ4686.

With the assumption that the He II orbit shown in Table 1 is from the companion star, and that the semi-amplitude from the higher-

order Balmer lines for the primary star (Grant et al. 2020), then the semi-amplitude ratio shows that the primary star is 2–3 times more massive than the secondary star. This is also an indicator that the companion is not likely a WNh star, as that would imply the primary star could have a mass of in excess of 100 $M_\odot$. Models of the system, such as those by Okazaki et al. (2008) and Madura et al. (2013), typically have the masses of the primary and secondary as 90 and 30 $M_\odot$ respectively, broadly in agreement with the kinematics of the orbits presented here. On the other hand, if η Carinae A has a mass of > 100$M_\odot$, the secondary would have a mass on the order of 50–60 $M_\odot$. This is similar to the nearby WNh star in the Carina nebula: WR22. The mass of this WNh star in an eclipsing system is 56–58 $M_\odot$ (Lenoir-Craig et al. 2022). The tidally-induced pulsations observed by Richardson et al. (2018) were modeled with stars of masses 100 and 30 $M_\odot$, and therefore may also support the higher masses suggested here.

Most models for η Car have a preferred orbital inclination of 130–145° (Madura et al. 2012), which agrees with forbidden [Fe III] emission observed with *Hubble Space Telescope*'s Space Telescope Imaging Spectrograph. This inclination can be used with the mass function derived from the primary star's orbit

$$f(M) = \frac{m_2^3 \sin^3 i}{(m_1 + m_2)^2} = (1.0361 \times 10^{-7})(1 - e^2)^{3/2} K_1^3 P[M_\odot]$$

to constrain the system's masses with the mass function using the standard units measured and our measured Hβ orbit using PHOEBE (Table 1). The mass function is $f(M) = 8.30 \pm 0.05$ M$_\odot$, and would indicate a companion star with a mass of at least 60 $M_\odot$ if we assume a primary mass of ∼ 90 $M_\odot$. Given the actual mass functions for the measured upper Balmer lines and He II orbits, the minimum masses required for these measured orbits are $M \sin^3 i = 102 M_\odot$ for the LBV primary and $M \sin^3 i = 55 M_\odot$ for the secondary, making the companion star's identification as a WNh star more likely. These results are still preliminary and require follow-up observations to constrain the orbits.

A WNh star can account for the mass of the secondary star in η Car, but could cause some difficulty for the modeling of the Great Eruption models of Hirai et al. (2021). In that scenario, the companion star would be a hydrogen-stripped star, contrary to the hydrogen content of the WNh stars. Recently modeled WNh systems such as R144 (Shenar et al. 2021) show that the surface fraction of hydrogen is about 0.4. This does show some amount of lost hydrogen on the surface, so the scenario could still be relevant even if the final star is not a fully stripped classical Wolf-Rayet star, assuming that the evolution of the secondary star has not been significantly influenced by mass exchange prior to or during the merger event hypothesized by both Portegies Zwart & van den Heuvel (2016) and Hirai et al. (2021).

6 CONCLUSIONS

In this paper, we provide an orbital ephemeris for η Carinae measured with a bisector method and high resolution ground-based spectroscopy of the Hβ emission line, along with an ephemeris for the He II λ4686 emission line at times far from periastron. Our findings can be be summarized as follows:

- The Hβ emission profile tracks the primary star, and our bisector method provides similar results as the multiple-Gaussian fitting method used by Grant et al. (2020). The results show a high eccentricity orbit of the system with the primary star in front of the secondary at periastron.

---

[3] http://pacrowther.staff.shef.ac.uk/WRcat/

• The weak He II λ4686 emission tracks opposite the kinematics of the primary star, suggesting it is formed in the secondary star's wind at times away from periastron. This could support the hypothesis of the scenarios presented by Hirai et al. (2021) for a stellar merger being the cause of the Great Eruption as the secondary could be a Wolf-Rayet star that has leftover hydrogen on its surface.

• With the assumed inclination of 130–145°, the masses of the stars could be around ∼100 $M_\odot$ for the primary and at least 60 $M_\odot$ for the secondary. However, the mass ratio derived by comparing the two semi-amplitudes is about 1.9. New observations will be needed to better determine precise masses.

Future studies will be able to better measure the He II 4686 orbit and refine its parameters. As shown in Grant et al. (2020), the upper Balmer lines are more likely to reflect the orbital motion of the stars, and the upper Paschen lines will also be useful. However, our work shows that a simpler bisector measurement of higher resolution spectroscopy results in the same derived orbital elements as that of Grant et al. (2020). Furthermore, with better signal-to-noise spectra, we can better determine if the He II emission near periastron can be reproduced with a Lührs model or if it is a signature of the companion. With this information, we will be able to more precisely measure the kinematics of the two stars and the mass function, and then we can begin to better understand the current evolutionary status of the system.

DATA AVAILABILITY

All measurements can be found in Appendix A. Reasonable requests to use the reduced spectra will be granted by the corresponding author.

REFERENCES

Aadland E., Massey P., Hillier D. J., Morrell N. I., Neugent K. F., Eldridge J. J., 2022, arXiv e-prints, p. arXiv:2204.04258

Barton C., Milson N., 2020, BinaryStarSolver: Orbital elements of binary stars solver, Astrophysics Source Code Library, record ascl:2012.004 (ascl:2012.004)

Corcoran M. F., Ishibashi K., Swank J. H., Petre R., 2001, ApJ, 547, 1034

Corcoran M. F., et al., 2017, ApJ, 838, 45

Currie D. G., et al., 1996, AJ, 112, 1115

Damineli A., 1996a, ApJ, 460, L49

Damineli A., 1996b, ApJ, 460, L49

Damineli A., Conti P. S., Lopes D. F., 1997, New Astron., 2, 107

Damineli A., Kaufer A., Wolf B., Stahl O., Lopes D. F., de Araújo F. X., 2000, ApJ, 528, L101

Damineli A., et al., 2019, MNRAS, 484, 1325

Damineli A., et al., 2021, MNRAS, 505, 963

Davidson K., 1997, New Astron., 2, 387

Davidson K., Humphreys R. M., 1997, ARA&A, 35, 1

Davidson K., Humphreys R. M., eds, 2012, Eta Carinae and the Supernova Impostors Astrophysics and Space Science Library Vol. 384, doi:10.1007/978-1-4614-2275-4.

Davidson K., Mehner A., Humphreys R. M., Martin J. C., Ishibashi K., 2015, ApJ, 801, L15

Espinoza-Galeas D., et al., 2022, ApJ, 933, 136

Fahed R., et al., 2011, MNRAS, 418, 2

Foreman-Mackey D., Hogg D. W., Lang D., Goodman J., 2013, PASP, 125, 306

Gaviola E., 1953, ApJ, 118, 234

Grant D., Blundell K., 2022, MNRAS, 509, 367

Grant D., Blundell K., Matthews J., 2020, MNRAS, 494, 17

Groh J. H., et al., 2010, A&A, 517, A9

Groh J. H., Hillier D. J., Madura T. I., Weigelt G., 2012, MNRAS, 423, 1623

Gull T. R., et al., 2022, ApJ, 933, 175

Hill G. M., Moffat A. F. J., St-Louis N., Bartzakos P., 2000, MNRAS, 318, 402

Hillier D. J., Crowther P. A., Najarro F., Fullerton A. W., 1998, A&A, 340, 483

Hillier D. J., Davidson K., Ishibashi K., Gull T., 2001, ApJ, 553, 837

Hirai R., Podsiadlowski P., Owocki S. P., Schneider F. R. N., Smith N., 2021, MNRAS, 503, 4276

Kashi A., Soker N., 2010, ApJ, 723, 602

Koenigsberger G., Moreno E., Langer N., 2021, A&A, 653, A127

Lenoir-Craig G., Antokhin I. I., Antokhina E. A., St-Louis N., Moffat A. F. J., 2022, MNRAS, 510, 246

Lührs S., 1997, PASP, 109, 504

Madura T. I., Groh J. H., 2012, ApJ, 746, L18

Madura T. I., Gull T. R., Owocki S. P., Groh J. H., Okazaki A. T., Russell C. M. P., 2012, MNRAS, 420, 2064

Madura T. I., et al., 2013, MNRAS, 436, 3820

Martin J. C., Davidson K., Humphreys R. M., Hillier D. J., Ishibashi K., 2006, ApJ, 640, 474

Mehner A., Davidson K., Martin J. C., Humphreys R. M., Ishibashi K., Ferland G. J., 2011, ApJ, 740, 80

Mehner A., et al., 2015, A&A, 578, A122

Milson N., Barton C., Bennett P. D., 2020, arXiv e-prints, p. arXiv:2011.13914

Morris P. W., Gull T. R., Hillier D. J., Barlow M. J., Royer P., Nielsen K., Black J., Swinyard B., 2017, ApJ, 842, 79

Nielsen K. E., Corcoran M. F., Gull T. R., Hillier D. J., Hamaguchi K., Ivarsson S., Lindler D. J., 2007, ApJ, 660, 669

Okazaki A. T., Owocki S. P., Russell C. M. P., Corcoran M. F., 2008, MNRAS, 388, L39

Paredes L. A., Henry T. J., Quinn S. N., Gies D. R., Hinojosa-Goñi R., James H.-S., Jao W.-C., White R. J., 2021, AJ, 162, 176

Pickett C. S., et al., 2022, arXiv e-prints, p. arXiv:2208.06389

Pittard J. M., Corcoran M. F., 2002, A&A, 383, 636

Pollock A. M. T., et al., 2021, ApJ, 923, 191

Portegies Zwart S. F., van den Heuvel E. P. J., 2016, MNRAS, 456, 3401

Prša A., Zwitter T., 2005, ApJ, 628, 426

Prša A., et al., 2016, ApJS, 227, 29
Richardson N. D., Gies D. R., Henry T. J., Fernández-Lajús E., Okazaki A. T., 2010, AJ, 139, 1534
Richardson N. D., Gies D. R., Gull T. R., Moffat A. F. J., St-Jean L., 2015, AJ, 150, 109
Richardson N. D., et al., 2016, MNRAS, 455, 244
Richardson N. D., et al., 2017, MNRAS, 471, 2715
Richardson N. D., et al., 2018, MNRAS, 475, 5417
Richardson N. D., et al., 2021, ApJ, 908, L3
Rosslowe C. K., Crowther P. A., 2015, MNRAS, 447, 2322
Shenar T., et al., 2017, A&A, 598, A85
Shenar T., et al., 2021, A&A, 650, A147
Smith N., et al., 2018, MNRAS, 480, 1466
Steiner J. E., Damineli A., 2004, ApJ, 612, L133
Teodoro M., et al., 2012, ApJ, 746, 73
Teodoro M., et al., 2016, ApJ, 819, 131
Thomas J. D., et al., 2021, MNRAS, 504, 5221
Tokovinin A., Fischer D. A., Bonati M., Giguere M. J., Moore P., Schwab C., Spronck J. F. P., Szymkowiak A., 2013, PASP, 125, 1336
Tramper F., et al., 2015, A&A, 581, A110
Vollmann K., Eversberg T., 2006, Astronomische Nachrichten, 327, 862
Weigelt G., Ebersberger J., 1986, A&A, 163, L5
Weigelt G., et al., 2007, A&A, 464, 87
Weigelt G., et al., 2021, A&A, 652, A140

APPENDIX A: APPENDIX

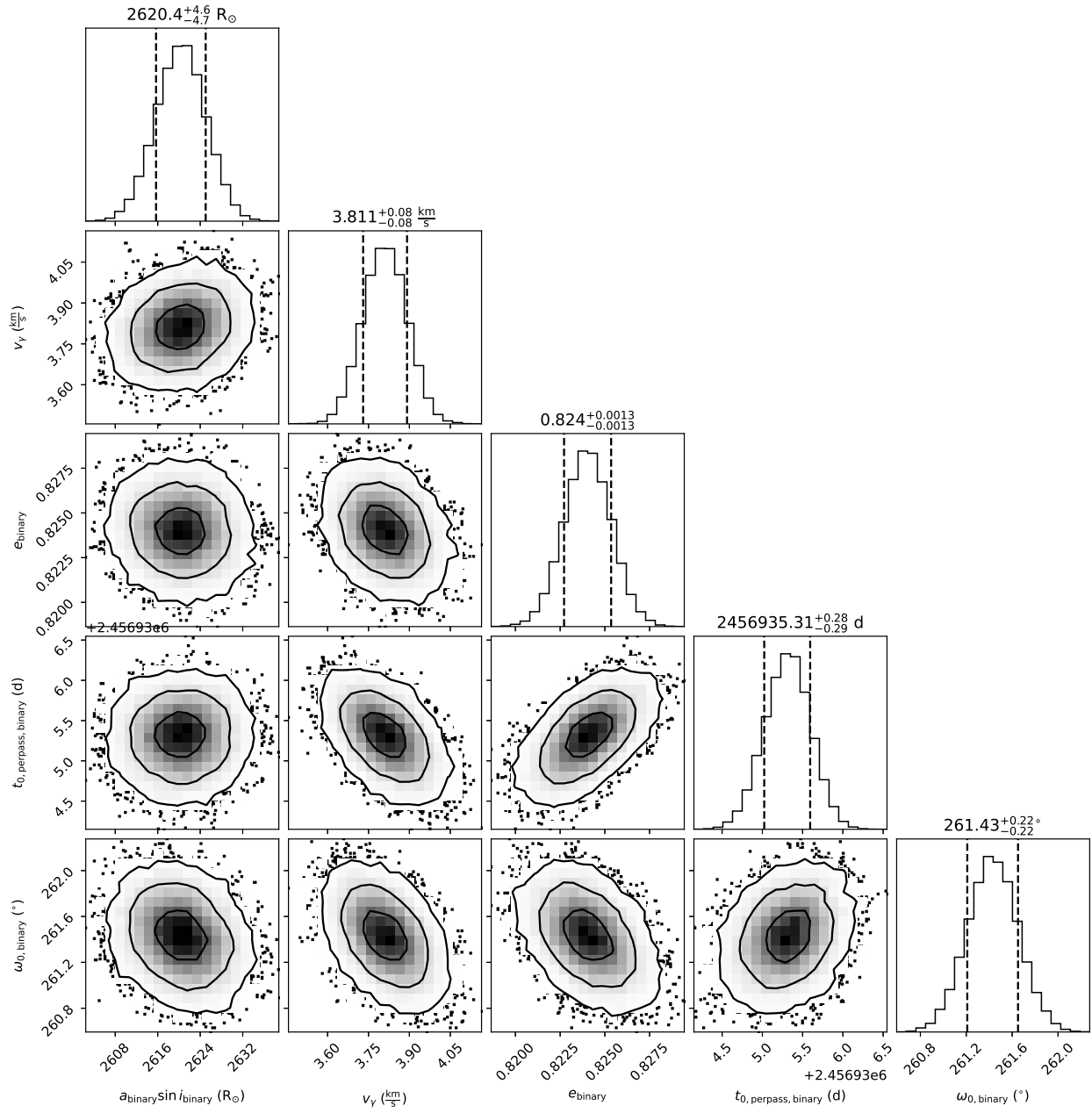This paper has been typeset from a TeX/LaTeX file prepared by the author.

Figure A1. Results of the Markov chain Monte Carlo fit for the Hβ velocities for only the data surrounding the 2014 periastron passage. Note that ω_0 refers to the value of ω for the primary star.